crystals

MDPI

Article

Effect of High-Energy Ball Milling in Ternary Material System of (Mg-Sn-Na)

Halit Sübütay [1] and İlyas Şavklıyıldız [2,*]

[1] Department of Metallurgical and Materials Engineering, Selçuk University, Konya 42075, Turkey; halit.subutay@selcuk.edu.tr
[2] Department of Metallurgical and Materials Engineering, Konya Technical University, Konya 42075, Turkey
* Correspondence: isavkliyildiz@ktun.edu.tr

Abstract: In this study, the nature of the ball-milling mechanism in a ternary materials system (Mg-6Sn-1Na) is investigated for proper mechanical alloying. An identical powder mixture for this material system is exposed to different milling durations for a suitable mixture. First, the platelet structure formation is observed on particles with increasing milling duration, mainly formed in <200> direction of the hexagonal crystal structure of the Mg matrix. Then, the flake structure with texture formation is broken into smaller spherical particles with further ball milling up to 12 h. According to EDS analysis, the secondary phases in the Mg matrix are homogenously distributed with a 12-h milling duration which advises a proper mixture in this material system. The solid solution formation is triggered with an 8-h milling duration according to XRD analysis on 101 reflections. Conventional sintering is performed at 350 °C in 2 h for each sample. In bulk samples, XRD data reveal that secondary phases (Mg_2Sn) with island-like structures are formed on the Mg matrix for a milling duration of up to 8 h. These bigger secondary phases are mainly constituted as Mg_2Sn intermetallic forms, which have a negative effect on physical and mechanical properties due to a mismatch in the grain boundary formation. However, the homogenous distribution of secondary phases with a smaller particle size distribution, acquired with 12 h milling time, provides the highest density, modulus of elasticity, and hardness values for this ternary materials system. The ternary materials produced with the 12-h ball-milling process provide an improvement of about 117% in hardness value compared with the cast form.

Keywords: Mg alloys; ball milling; mechanical alloying; ternary material system

Citation: Sübütay, H.; Şavklıyıldız, İ. Effect of High-Energy Ball Milling in Ternary Material System of (Mg-Sn-Na). *Crystals* **2023**, *13*, 1230. https://doi.org/10.3390/cryst13081230

Academic Editor: Jacek Ćwik

Received: 27 July 2023
Revised: 4 August 2023
Accepted: 8 August 2023
Published: 9 August 2023

1. Introduction

Magnesium and its alloys are the lowest mass density morphological materials with well-shapeable and high-wear resistance, which makes them potential candidates for several applications such as aircraft, biomaterials, and automobiles [1,2]. The primary downside of Mg is its low formability at decreasing temperatures due to the limited activation of shear systems [3]. In addition, another disadvantage is the very low corrosion resistance of Mg [4]. Alloying process for pure Mg is a proper solution for strengthening, raising formability, and improving the corrosion resistance of magnesium alloys [5–7]. The alloying effect of such elements as Ti [8], Cu [9], Al [10], Ni [11], Sn [12], Zn [13], Ca [14], Zr [15], and Mn [16], or such rare earth elements as Ce [17], Sm [18], Dy [19], Er [20], and Y [21], have been commonly employed in Mg and alloys. Such alloying processes and thermomechanical processing, such as high-energy ball milling, have provided a significant enhancement in specific endurance, sinterability, and creep properties [22].

A high-energy ball-milling process, which provides mechanical alloying (MA), is used as the most common method for alloying powders, in which different material systems can mix homogeneously at the ppm level due to the involvement of the continuous cold-welding and fracturing mechanisms [23]. The most common issue in the high-energy

ball-milling procedure is a continuous collision between ball-powder jar, which leads to severe plastic deformations on particles [24] and fracture of the platelet particles, causing the variation of lattice strain, crystallite size, and attaining nano-sized structures and phase transformations [25,26]. After mechanical alloying due to reiterative fracture, cold welding, and refracture of powders, new effective surfaces improve chemically, and supersaturation may occur beyond the equilibrium limit [27]. Furthermore, thermomechanical activation of the particle morphology plays a significant role in the high-energy ball-milling process [28]. In the literature, there are publications reporting that the solubility of Titanium in Mg [29] and Magnesium in Ti [30] in studies with mechanical alloying Ti-Mg powders increases. High-energy ball milling is used in the production of composite materials with high physical and mechanical properties, which are complex and expensive to manufacture with traditional methods such as casting [31].

According to the literature survey [32–37], it is clearly seen that several composite materials are manufactured by changing matrix and reinforcement species with different particle size distribution in conjunction with altering milling conditions, such as milling time and processing agent [38]. Wang et al. [39] investigated Mg-%25 wt. Sn composite alloys manufactured by mechanical alloying. They reported that sintering parameters and the number of secondary phases directly affect the mechanical properties by changing the ball-milling duration.

Son et al. [40] studied the relationship between precipitation nature and mechanical properties of multiphase of Mg-Sn-Al-Zn alloys. The intermetallic phases, such as Mg_2Sn, have a major effect on the development of mechanical properties. The creep endurances of binary Mg-Sn and ternary Mg-Sn-Al material systems were studied by Poddar et al. [41], which suggested that the creep behavior of the materials could be developed with the help of intermetallic phases, including Mg_2Sn, which has chemical stability at higher temperatures [42]. Mendis et al. [43] surveyed the role of Na addition to Mg-Sn alloys alloyed by the casting method. In their study, it was clearly seen that an abnormal increase in hardness occurred because the distribution of Na led to an increment in the number of intermetallic precipitates.

Although different studies on Mg-Sn composite alloys fabricates via casting and powder metallurgy are well tabulated in the literature, there is a limited experimental investigation of the effect of the milling time and addition of trace amount Na element on the powder morphology, precipitate formation, intermetallic transformation, and crystallographic properties of high-energy ball-milled Mg-Sn-Na metal powders and their relationship between density, hardness, elastic module of generated composite alloys [44]. For this reason, the main aim of the study is to do an elaborate characterization of powder morphology, the variation of crystallite size, the distribution of reinforcement species (Sn and Na), and the occurrence of Mg_2Sn intermetallic formation with the addition of Na element within the Mg matrix. Moreover, sintered Mg-Sn-Na composite alloys are employed to examine densities, hardness, and elastic modulus.

2. Materials and Methods

2.1. Materials and Ball-Milling Process

In the present study, Sn (6 wt%) and Na (1 wt%) were used to reinforce elements in the Mg matrix to produce alloys with metal matrix. Pure Mg (<53 μm; 99.99 wt% purity) and Sn (<6 μm; 99.9 wt% purity) elemental powders were obtained by Nanografi Company(Ankara, Turkey). Mg, Sn, and Na powders were high-energy ball-milled with tungsten carbide (WC; 10 mm diameter) balls in a tungsten carbide jar (250 mL) using RETSCH-PM 100 (Konya, Turkey) planetary ball-milling device at a rotation speed of 250 rpm.

The ball-to-powder (BPR) massive 5:1 rate was chosen, and the ball-milling time was selected as 0.5, 2, 4, 8, and 12 h. To prevent clusters, cold working, and severe plastic deformation of the powders' duration milling, 4 wt% stearic acid was used as a process control agent (PCA). To avoid excessive temperature rise throughout the ball-milling time,

the device was milled for 5 min, then rested for 5 min. After ball milling, the powders were compacted under 500 MPa pressure for 30 s by a cold-press device. To prevent oxidation, all green compacts (cold-pressed specimens) were sintered for 2 h at 350 °C with a stable heating rate of 5 °C/min under the high-purity argon atmosphere. The argon flow ratio was constant at 3 L/min. In Figure 1, the preparation and production of Mg-Sn-Na alloy is represented schematically.

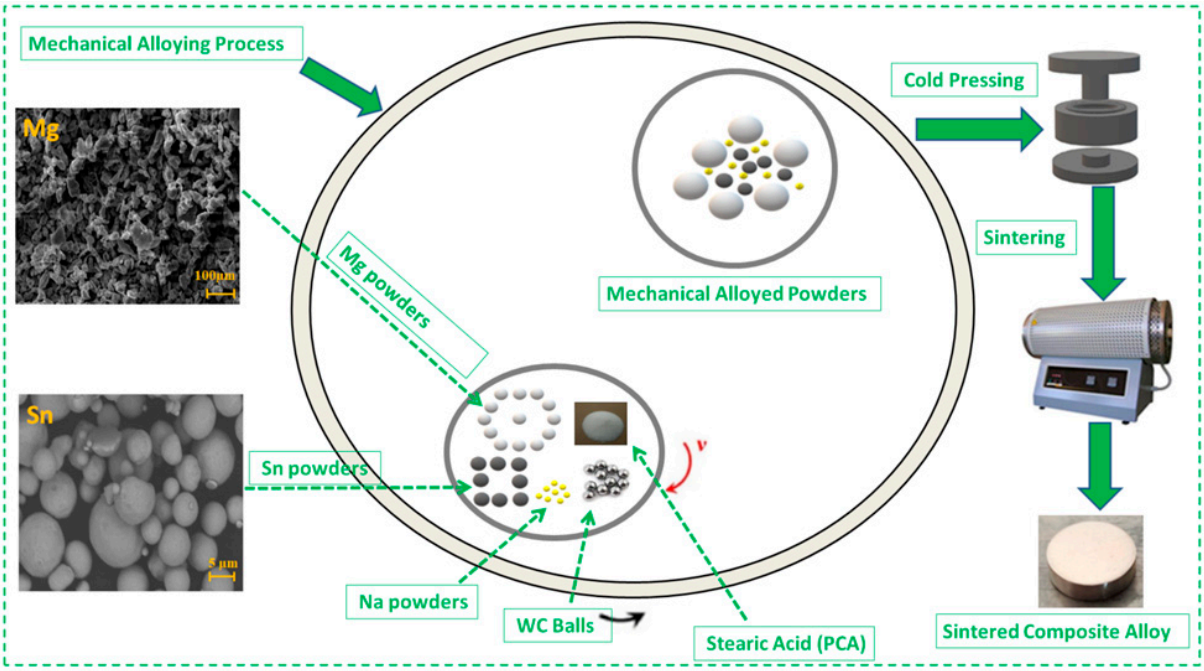

Figure 1. Schematic experimental setup for ball milling and Powder Metallurgy procedure.

2.2. Powder and Sintered Sample Characterization

The morphologies of milled and unmilled powders, along with microstructural progress in sintered composite alloys, were investigated using scanning electron microscopy (SEM, Zeiss EVO LS10, Konya, Turkey). Elemental analysis of the milled powders and dispersion mechanism of sintered composite alloys were investigated with EDS-Mapping and line scan mode. Moreover, all ball-milled powders' particle size distribution (PSD) was examined via a Mastersizer particle size analyzer device. X-ray diffractometer (XRD) was utilized to calculate the crystallite size and define the peak profile parameters. XRD data were gathered by Cu-radiation at wavelength of 1.5406 Å by utilizing a step-scan procedure with 0.15 degrees 2-theta at every step and 4 s at every step dwelling time [45]. Peak profile parameters of all ball-milled powders were detected by the MDI Jade XRD program. For all ball-milled powders, the Debye Scherrer equation was utilized to calculate values of lattice strain and crystallite size (Equation (1)) [46].

$$D_{hkl} = \frac{K \times \lambda}{(\beta_{hkl} \times cos\Phi)} \quad (1)$$

where K (0.94) is the shape coefficient; λ is the wavelength of Cu radiation; β is the FWHM value of the peak, and Φ is the XRD diffraction angle [47,48].

Dislocation density (δ) values were calculated according to Williamson–Smallman formula given in Equation (2) [48,49].

$$\delta = n/D^2 \quad (2)$$

Here, n is nearly 1, and D is the crystallite size. Theoretical density values of sintered composite alloys were calculated utilizing the mixture rule formula, and their experi-

mental density measurements were carried out according to the ASTM B962-17 standard Archimedes' principle [50]. The microhardness values of the sintered composite alloys were surveyed via a micro-Vickers hardness measure procedure. The micro-Vickers hardness test [51] was performed under an applying load of 10 gf and a dwelling time of 20 s. At least five measurements were taken for the average hardness value.

Young's Modulus of sintered composite alloys was used to calculate the ultrasonic wave velocity (UWC) measurement method [48]. UWC measurements were performed in tangency mode to strengthen ASTM E494-20, utilizing the ultrasonic pulse-echo-overlap method (PEOM) [52]. The UWC measurements were carried out utilizing one flaw detector, one-number longitudinal wave tangency transducer (20 MHz), and one-number shear-wave tangency transducer (5 MHz) [53].

3. Results and Discussion

3.1. Powder Morphology

At first glance, the particle morphology of the ternary material system of (Mg-Sn-Na) is preserved after the 0.5 h milling process. In Figure 2, the particles show a spherical form as the initial powder mixture. So, 0.5 h milling duration has almost no effect on the change in both particle morphologies and in the mixing nature of the ternary system, which arouses the need for further milling for proper mixing. Then, the said material system is exposed to a 2-h ball-milling treatment. The flake shape of particles is a sign that the ball-milling procedure in this material system works efficiently, along with extreme plastic deformation. The particles turn into flake structures due to continuous collision between ball–ball and ball–wall with increasing surface area and particle size of up to 70 microns. Furthermore, few cold-welding mechanisms are observed between the small particles and bigger particles. However, the 4-h milling procedure triggers a huge cold-welding mechanism that involves flake particles due to excessive plastic deformation on particles. Eventually, all welded particles create platelet structure formation with an increasing particle size of up to 120 microns, which tripled the initial powder particle size distribution. After this point, the particles start to break into much smaller forms, which is attributed to severe work hardening with further ball milling of up to 8 h in duration. Bigger platelet particles with small broken pieces create a bimodal particle size distribution, as seen in Figure 2. During high-energy ball milling, cold working and fracture mechanism work concomitantly for proper mechanical alloying. However, after a certain milling duration, the fracture mechanism becomes the dominant instrument for the particles, which is due to either extreme work hardening or loss of function of the processing agent. With an 8-h milling process, all particles are exposed to severe plastic deformation and accumulate excessive stress concentration, which eventually affects the sinterability of this material system. Further high-energy ball-milling process of up to 12 h turns the flake morphology into smaller fragmented particle formations. Monomodal particle size distribution is also revealed with 12-h milling time, and particle size distribution of milled powder of less than 10 microns is received, which is well below the initial particle size. The final microstructure formation suggests that a 12-h milling duration is enough to provide sufficient mixing and mechanical alloying for this ternary material system.

The EDS analysis represented in Figure 3 also verifies the homogenous mixture of the ternary system. All elements (Mg-Sn-Na) in this system are uniformly dispersed throughout the sample. However, our previous study revealed that monomodal particle size distribution was acquired via an 8-h milling duration in a binary system of (Mg-9Sn) [48]. So, the presence of Na elements in this ternary system prevents or retards the fracture mechanism, and an extra 4-h milling process is needed to achieve homogenous mixing formation with smaller particle size distribution.

The particle size analyses also show the same tendency regarding particle evolution as a function of milling time. First, the nature of the single peak at higher numbers advises that the particle size is increased with monomodal distribution in this material system up to 4 h of the milling procedure (Figure 4). Then, the bimodal distribution observed

within 8 h leads to two separated peaks, according to the particle analyzer. Finally, a single intense peak profile is acquired around the 10-micron range, with 12 milling durations. Overall, the particle size analysis is consistent with SEM micrograph examination, as explained previously.

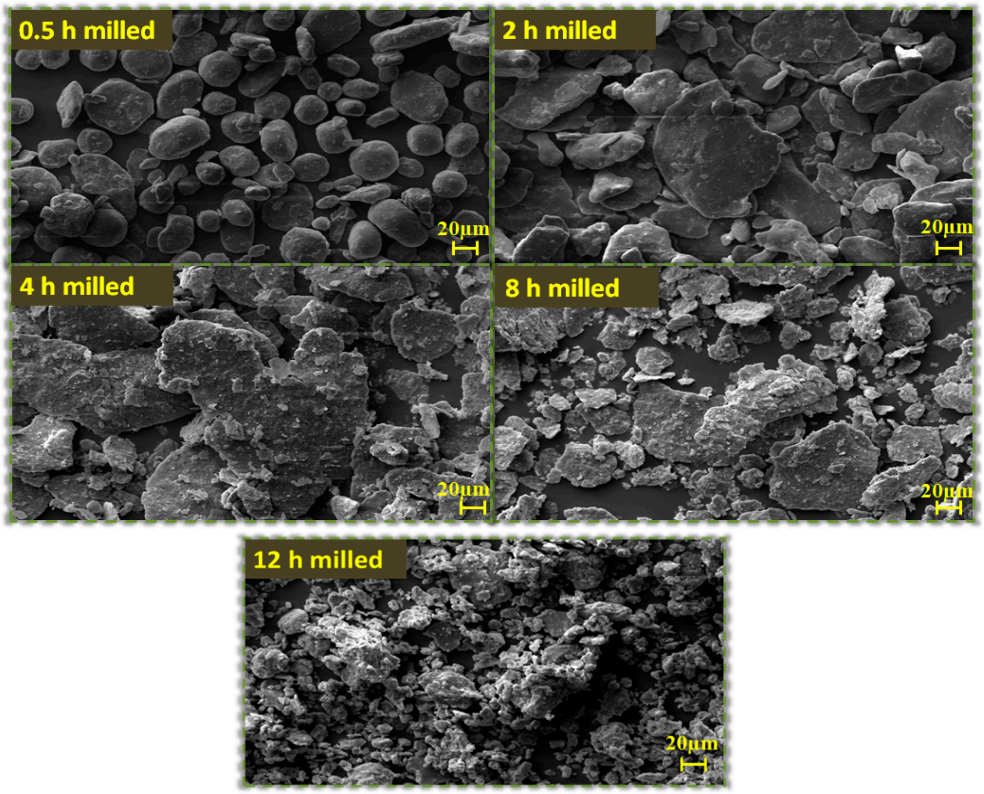

Figure 2. SEM examination of ball-milled Mg-6Sn-1Na powders at particular milling duration.

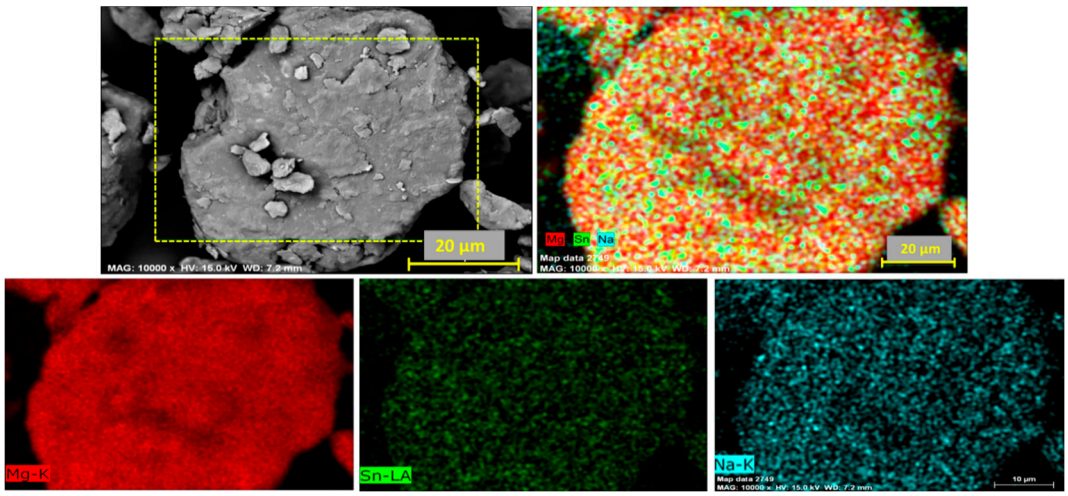

Figure 3. EDS mapping analysis for ball-milled powder at 12-h milling duration.

XRD analysis also helps to understand both phase formation and peak profile evolution for each phase, as represented in Figure 5. Peaks for Mg and Sn phases are detected in up to 2 h of milling conditions. However, the 4-h milling duration makes Sn peaks fade out, and the intermetallic phase of Mg_2Sn starts to appear in the XRD spectrum. This behavior is attributed to the high-energy ball-milling work. So, at least 4-h ball milling needs to trigger

intermetallic formation in this system. However, in the Mg-Sn binary system, such behavior was achieved in the 2-h milling procedure, which means that the presence of Na also delays the formation of the intermetallic phase [54,55]. Further ball-milling process maps the Sn out from the XRD spectra, as observed in the 8-h and 12-h conditions. Such observation suggests that the Sn phase goes into both solid solutions in the Mg matrix and chemical reaction for intermetallic phase formation [56]. A closer approach to the major peak (101) of the Mg phase is represented in Figure 5c. The peak position of (101) reflection first has a tendency to shift to higher degrees, which intimates the decrement in the interatomic distance because of the compression stress [57]. A repetitive collision during the milling process creates such compression stress formation on particles as a natural high-energy ball milling. This issue is the case for the milling condition for up to 4-h duration. After that, the 101 peaks start to shift to lower degrees, which means that the interatomic distance for this reflection starts to increase [58]. This singularity is only due to the solid solution formation in the Mg matrix in this case [59]. It is important to state that Na and Sn elements are initiated to dissolve into the Mg matrix due to the high-energy ball milling in the 8-h conditions. Therefore, at least an 8-h milling procedure is needed to trigger solid solution formation in the ternary (Mg-Sn-Na) material system. Nonetheless, in the binary material system of (Mg-9Sn), solid solution formation was observed with a 4-h ball milling [48]. So, the existence of the Na element also postpones the solid solution formation. The peak intensity of (101) reflection is monolithically reduced with increasing milling duration, which advises the reduction in crystallite size or coherent diffraction in domain size. The continuous collision mechanism during ball milling leads crystals to break apart in the (101) direction. Regarding the (002) reflection of the Mg matrix, the (002) reflection shows singularity in terms of peak intensity changes. Peak intensity first starts to increase with the increase in milling duration of up to 4 h and also shows higher relative peak intensity than the major peak (101) reflection of the Mg matrix. Such a result is attributed to the texture formation in a hexagonal crystal structure of Mg. Therefore, we conclude that severe plastic deformation observed in the SEM micrograph is mainly elongated through the (002) direction. Because the interatomic bonding governed in this direction is weak, atoms prefer to be oriented accordingly [60–62]. A further ball-milling process results in a decrease in the peak intensity of (002) reflection, which refers to breaking the coherent diffraction domains for the (002) reflection.

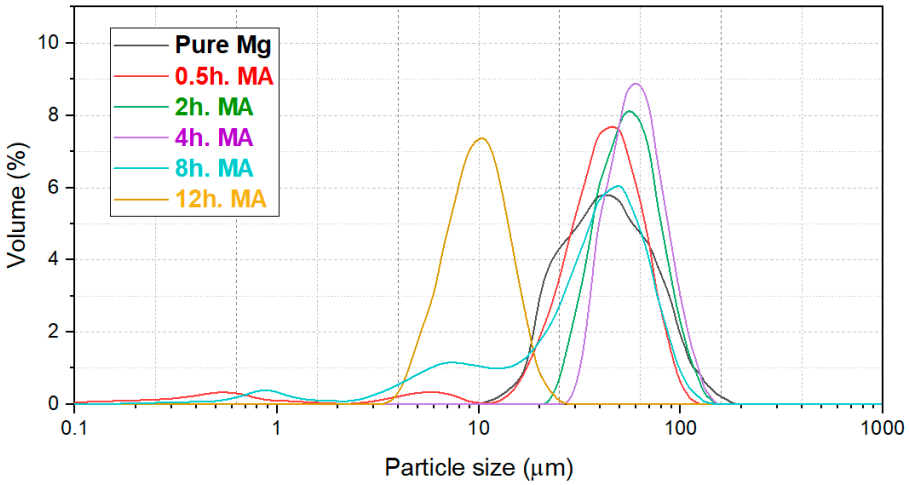

Figure 4. Particle size distribution of each sample, ball milled at different durations.

The crystallite size is also decreased as the particles break apart, as observed in SEM analysis. So, SEM micrograph analysis supports the XRD data analysis. The changes in crystallite size for the (002) reflection are inconsistent with the particle size variation as a function of the milling time. As represented in Figure 6, the crystallite size improved from 43 nm to 63 nm with the increasing milling duration of up to 4 h, according to

the calculation with the (002) peak reflection parameters. On the contrary, the dislocation density and localized lattice strain are reduced as expected. However, a prolonged milling procedure of up to 12 h has a negative effect on crystallite size variation, and the crystallite size of the final powder is measured at 40 nm, which is lower than at the initial stage. Lattice strain and dislocation density values are increased up to %0.29 and 0.62×10^{15} line/m^2, respectively.

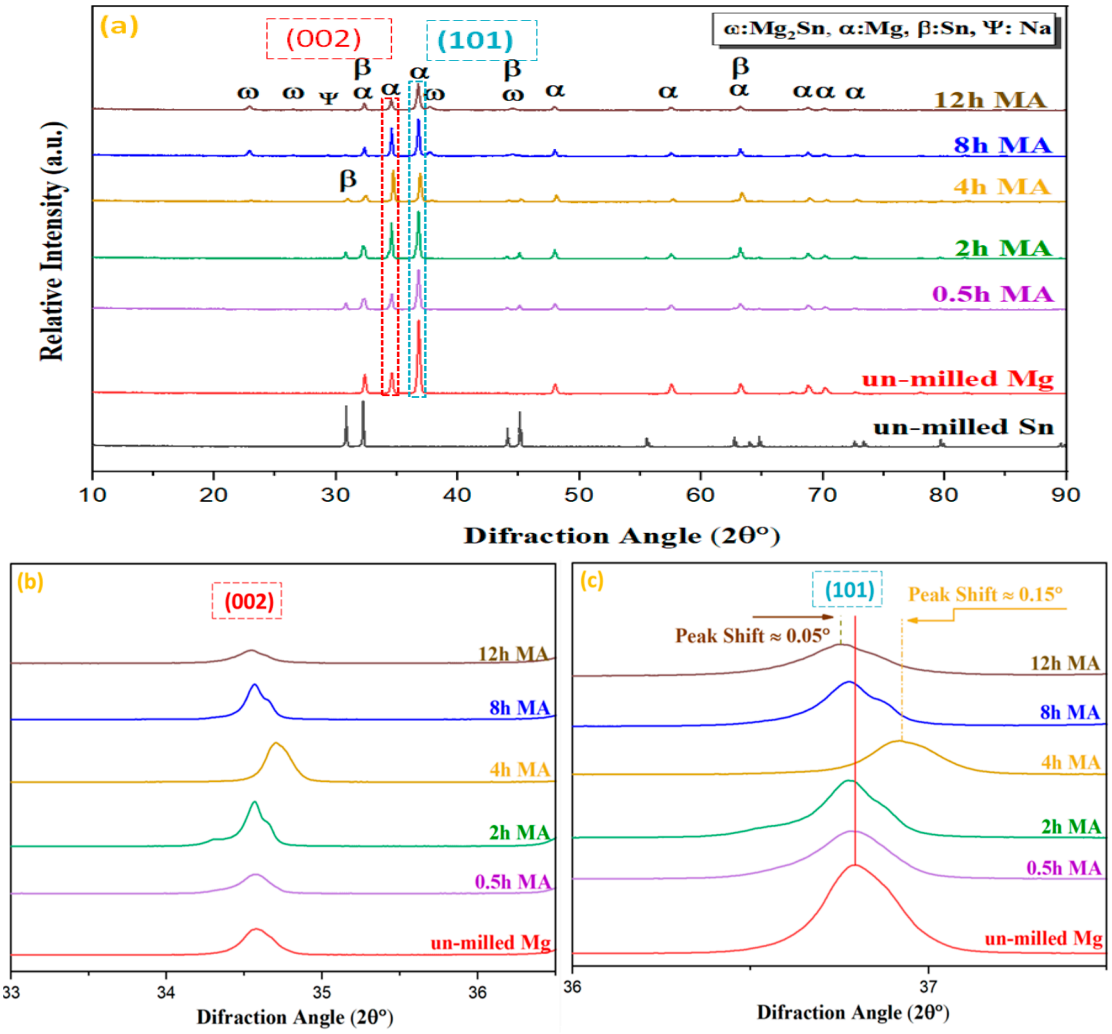

Figure 5. XRD analysis for all samples (**a**) and peak profile evolution on (002) (**b**) and (101) (**c**) reflection for different milling durations.

3.2. Bulk Material Characterization

The SEM micrograph examination, along with the elemental line scan analysis, is illustrated in Figure 7 with different milling durations. Secondary phases in the Mg matrix appear in a lighter color in SEM illustration due to the higher atomic number of Sn element. Agglomerated secondary phase existence on the Mg matrix is observed for all conditions except 12 milling durations. Secondary phases also precipitate vicinity of grain boundaries. Individual secondary phases create their island structure on the Mg matrix with a range of 40–60 microns. This behavior of the secondary phase suggests that the ball-milling process of up to 8 h does not provide a proper mixture in the Mg-Sn-Na material system. However, the microstructure of the 12-h milled conditions conveys a homogenously dispersed secondary phase with a smaller size in the Mg matrix. It is important to have homogenously distributed secondary phases to have improved physical and mechanical properties for multiphase material systems. According to our previous

study, the homogenous distribution of the secondary phase in a binary Mg-Sn composition reached an 8-h milling condition, which advised that the existence of the Na phase also delayed the homogenous mixing. Line scan for each condition is collected via both the Mg matrix and the secondary phase. The lighter area in the SEM illustration has a higher concentration of the Sn phase with the Mg phase's existence, which suggests that the island structure secondary phases are mainly the Mg_2Sn intermetallic phases, as detected via the XRD analysis as well. The line scan also reveals surprising results regarding the existence of Na in this material system. Na elements mainly precipitate on grain boundary instead of dissolving into an Mg matrix to create the solid solution. This situation of Na elements could have an important role in this ternary material system to improve mechanical properties by providing a precipitation hardening mechanism. EDS mapping analysis for the 12-h condition shows the homogenous distribution of each phase with no impurities, as represented in Figure 8.

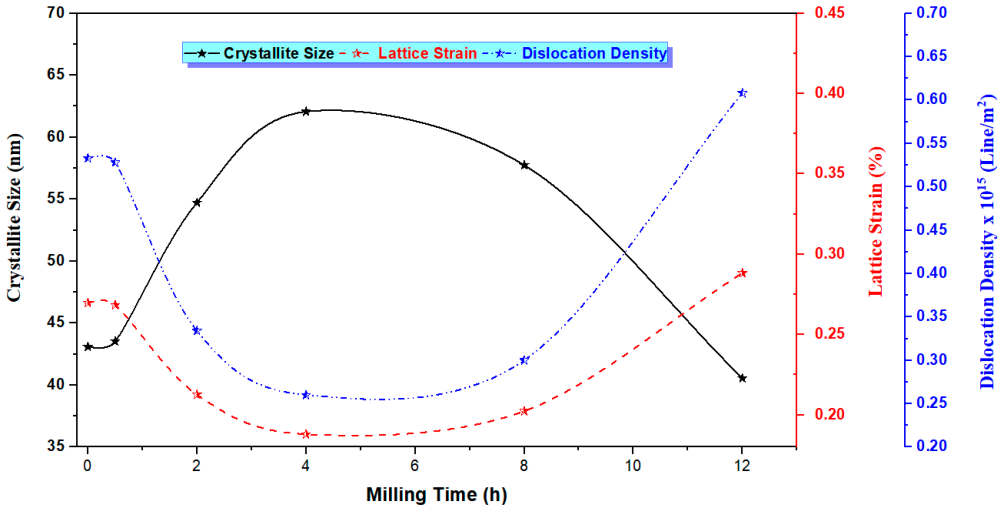

Figure 6. Illustration of changes for crystallite size, lattice strain, and dislocation density at different milling times.

Figure 9 represents the hardness value variation of sintered milled powders at different milling durations. The hardness values at first tend to increase with increasing milling process. However, an 8-h ball-milling duration has a negative effect on this trend, and the hardness value decreases in an 8-h milling duration. Then, the hardness value reaches the highest value of 90 HV for the 12-h milling condition. The increment in hardness value has a correlation with the milling duration because the higher milling duration generally provides homogenous mixing and dispersion of the additive elements in the Mg matrix. As explained before, the SEM micrograph examination on bulk samples suggests that the island-like precipitation of the secondary phase is observed instead of the homogenous dispersion in the matrix [63]. So, the incompatibility at the interface between the bigger secondary phase and matrix is the weak point, which reduces the mechanical properties [63–65]. The bigger size of the secondary phase creates a transition between small angles to high-angle interface formation [25,66] through the grain boundaries. Another explanation for variation in the mechanical properties is the Orowan mechanism, which is also involved and eventually affects the mechanical properties of the end product [67]. The slight reduction in the 8-h milling conditions can be explained by both the initial powder structure and the microstructure formation of bulk or sintered samples. The powder form of the 8-h condition suggests the bimodal particle size distribution. Repetitive collision in the ball-milling process results in a high-stress concentration in particles, which eventually hinders the diffusion or mass transport during the sintering procedure [68]. So, the density, elastic modulus, and hardness values for the 8-h condition are decreased. The second reason causing this disparity is the generation of a secondary phase in the Mg matrix

after the sintering process. As explained, the island-like formation of a secondary phase instead of homogenous distribution causes the diminishment in physical and mechanical properties. According to the previous study, the hardness value for the binary system of Mg-Sn was found to be 71.2 HV [48], but in this ternary system, the hardness value is improved to the 90 HV range (Figure 9). So, the presence of Na element in grain boundaries causes such an impact on hardness by triggering a precipitation hardening mechanism [69,70]. The elasticity modulus and density values for this material system show the same behavior as the hardness values. The density value for each sample is the sign of the sinterability of the milled powder, which is determined by the ball-milling duration in this study. So, the particle morphology and the nature of mixing of secondary phases in the matrix are the parameters determining the sinterability of the powder. Overall, the highest density and modulus of elasticity are acquired as 96% and 36 GPa for the 12-h milling condition (Figure 10). In this material system, the Na element has a huge effect on powder morphology, which eventually determines the physical and mechanical properties of bulk samples.

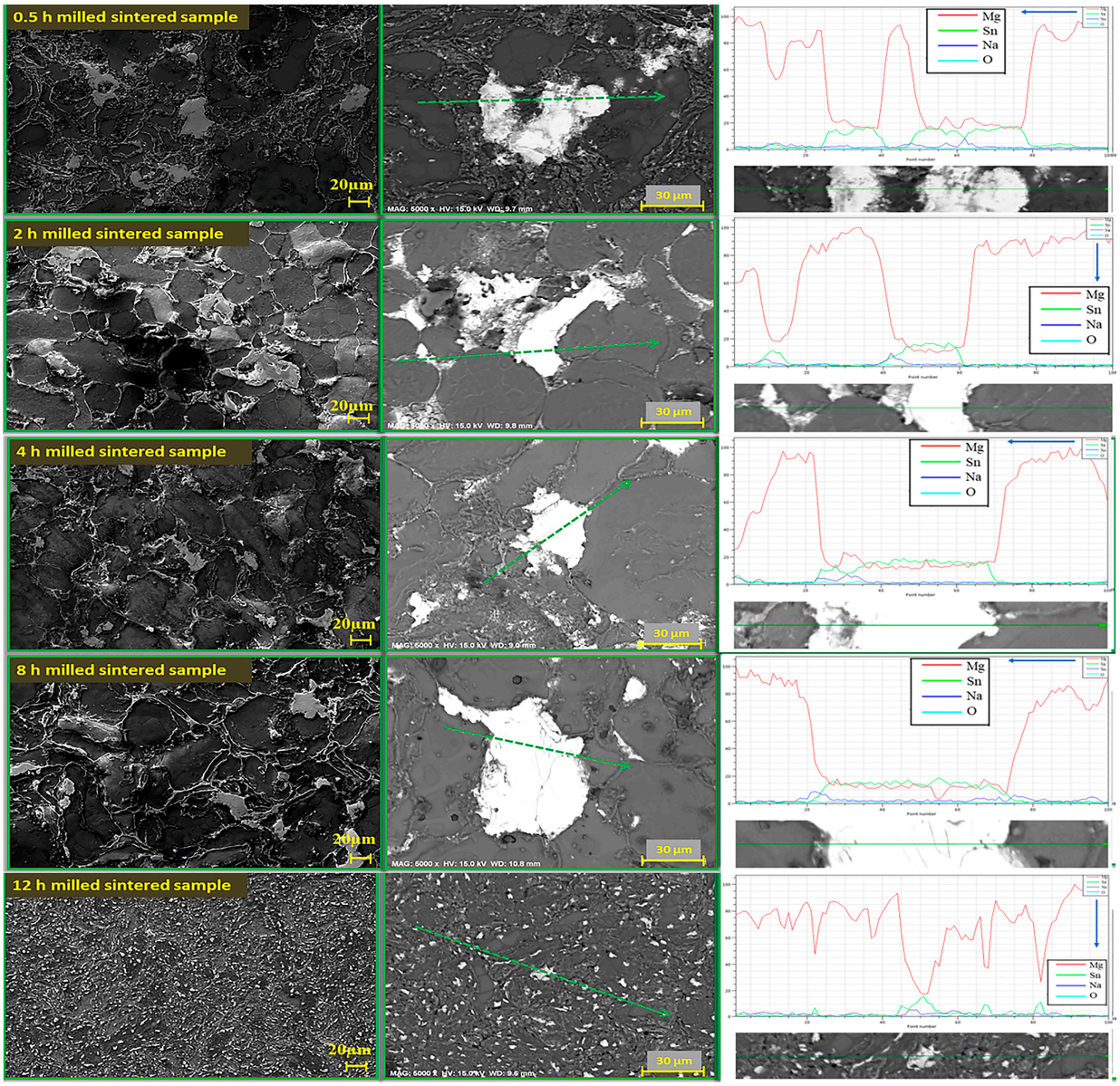

Figure 7. SEM micrograph representation on bulk ternary material system (Mg-Na-Sn) as a function of milling time.

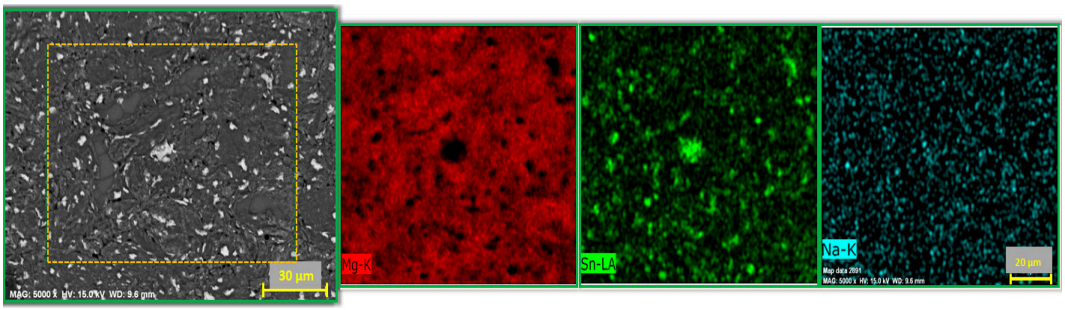

Figure 8. Mapping analysis of 12-h ball-milled 6 wt% Sn-Na-Mg sintered composite alloy.

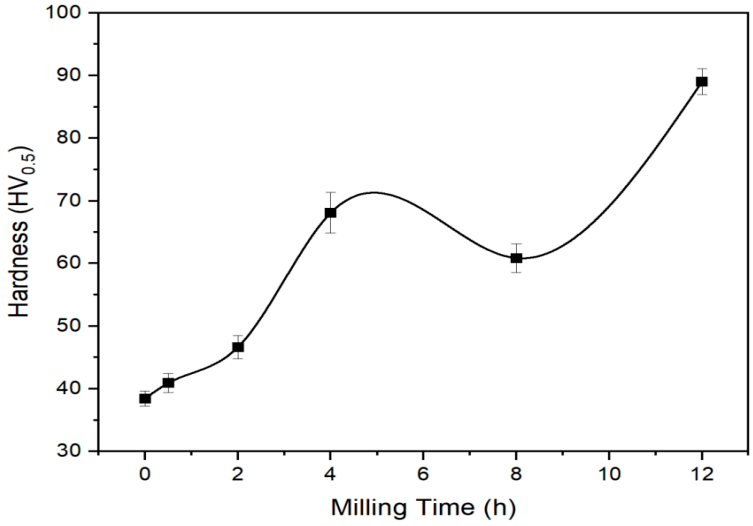

Figure 9. Representation of hardness values with different milling duration.

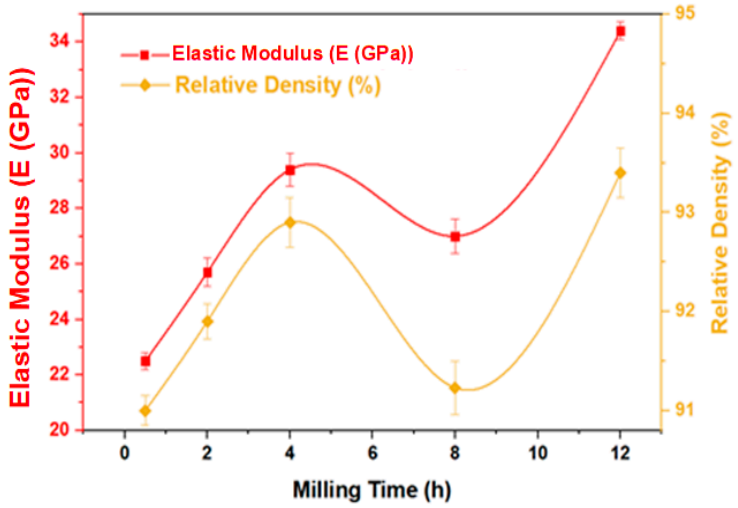

Figure 10. Variation of relative density and elastic modulus as a function of milling duration.

4. Conclusions

In this study, we aim to have a proper solid solution and mechanical alloying in the ternary system of (Mg-Sn-Na) by changing high-energy ball-milling duration. The following outcomes are acquired according to our experimental results:

- The milling process first causes the formation of platelet structure in this material's composition. Then, a further milling process of up to 12 h leads to breaking the flake form of powders into small spherical particles with monomodal distribution;

- XRD data reveal that the Sn phase starts to both dissolve and involve a chemical reaction for intermetallic phase (Mg_2Sn) formation with an 8-h milling condition;
- X-ray diffractometry study on (002) reflection of the Mg phase conveys the texture formation in the Mg matrix, which helps us to understand the nature of the platelet structure, as observed in SEM micrograph examination;
- The island structure of the secondary phase affects the physical and mechanical properties of bulk or sintered samples for samples milled up to 8 h;
- In 12 milling conditions, the homogenous secondary phase distribution is achieved, which eventually supplies the highest relative density (95%), modulus of elasticity (34.5 GPa), and hardness (89 HV) values in this ternary material system.

Author Contributions: H.S., investigation, methodology, data curation, writing—original draft; İ.Ş., investigation, conceptualization, supervision, writing—review and editing. All authors have read and agreed to the published version of the manuscript.

Funding: The financial support provided to this study by the Scientific Research Projects Coordination Unit (SRPCU) of Selçuk University through contract# 18401032 and the Scientific Research Projects at Konya Technical University through contract# 191019035.

Institutional Review Board Statement: Not applicable.

Informed Consent Statement: Not applicable.

Data Availability Statement: Not applicable.

Conflicts of Interest: The authors declare no conflict of interest.

References

1. Aalipour, Z.; Zarei-Hanzaki, A.; Moshiri, A.; Abedi, H.; Waryoba, D.; Kisko, A.; Karjalainen, L. Strain dependency of dynamic recrystallization during thermomechanical processing of Mg–Gd–Y–Zn–Zr alloy. *J. Mater. Res. Technol.* **2022**, *18*, 591–598. [CrossRef]
2. Zhong, X.; Wong, W.; Gupta, M. Enhancing strength and ductility of magnesium by integrating it with aluminum nanoparticles. *Acta Mater.* **2007**, *55*, 6338–6344. [CrossRef]
3. Koike, J.; Kobayashi, T.; Mukai, T.; Watanabe, H.; Suzuki, M.; Maruyama, K.; Higashi, K. The activity of non-basal slip systems and dynamic recovery at room temperature in fine-grained AZ31B magnesium alloys. *Acta Mater.* **2003**, *51*, 2055–2065. [CrossRef]
4. Atrens, A.; Song, G.-L.; Cao, F.; Shi, Z.; Bowen, P.K. Advances in Mg corrosion and research suggestions. *J. Magnes. Alloys* **2013**, *1*, 177–200. [CrossRef]
5. Kwak, T.; Kim, W. Effect of refinement of grains and icosahedral phase on hot compressive deformation and processing maps of Mg–Zn–Y magnesium alloys with different volume fractions of icosahedral phase. *J. Mater. Sci. Technol.* **2019**, *35*, 181–191. [CrossRef]
6. Zhao, C.; Pan, F.; Zhao, S.; Pan, H.; Song, K.; Tang, A. Preparation and characterization of as-extruded Mg–Sn alloys for orthopedic applications. *Mater. Des.* **2015**, *70*, 60–67. [CrossRef]
7. Jiang, W.; Wang, J.; Zhao, W.; Liu, Q.; Jiang, D.; Guo, S. Effect of Sn addition on the mechanical properties and bio-corrosion behavior of cytocompatible Mg–4Zn based alloys. *J. Magnes. Alloys* **2019**, *7*, 15–26. [CrossRef]
8. Tejeda-Ochoa, A.; Kametani, N.; Carreño-Gallardo, C.; Ledezma-Sillas, J.; Adachi, N.; Todaka, Y.; Herrera-Ramirez, J. Formation of a metastable fcc phase and high Mg solubility in the Ti–Mg system by mechanical alloying. *Powder Technol.* **2020**, *374*, 348–352. [CrossRef]
9. Cheng, J.; Cai, Q.; Zhao, B.; Yang, S.; Chen, F.; Li, B. Microstructure and Mechanical Properties of Nanocrystalline Al–Zn–Mg–Cu Alloy Prepared by Mechanical Alloying and Spark Plasma Sintering. *Materials* **2019**, *12*, 1255. [CrossRef]
10. Singh, D.; Suryanarayana, C.; Mertus, L.; Chen, R.-H. Extended homogeneity range of intermetallic phases in mechanically alloyed Mg–Al alloys. *Intermetallics* **2003**, *11*, 373–376. [CrossRef]
11. Fadonougbo, J.O.; Kim, H.-J.; Suh, B.-C.; Yim, C.D.; Na, T.-W.; Park, H.-K.; Suh, J.-Y. On the long-term cyclic stability of near-eutectic Mg–Mg_2Ni alloys. *Int. J. Hydrogen Energy* **2022**, *47*, 3939–3947. [CrossRef]
12. Zhong, H.; Xu, J. Tuning the de/hydriding thermodynamics and kinetics of Mg by mechanical alloying with Sn and Zn. *Int. J. Hydrogen Energy* **2019**, *44*, 2926–2933. [CrossRef]
13. Lesz, S.; Hrapkowicz, B.; Karolus, M.; Gołombek, K. Characteristics of the Mg–Zn–Ca–Gd Alloy after Mechanical Alloying. *Materials* **2021**, *14*, 226. [CrossRef] [PubMed]
14. Raducanu, D.; Cojocaru, V.D.; Nocivin, A.; Hendea, R.; Ivanescu, S.; Stanciu, D.; Trisca-Rusu, C.; Drob, S.I.; Cojocaru, E.M. Mechanical Alloying Process Applied for Obtaining a New Biodegradable Mg–xZn–Zr–Ca Alloy. *Metals* **2022**, *12*, 132. [CrossRef]

15. Al-Aqeeli, N.; Mendoza-Suarez, G.; Suryanarayana, C.; Drew, R. Development of new Al-based nanocomposites by mechanical alloying. *Mater. Sci. Eng. A* **2008**, *480*, 392–396. [CrossRef]
16. Lala, S.; Maity, T.; Singha, M.; Biswas, K.; Pradhan, S. Effect of doping (Mg, Mn, Zn) on the microstructure and mechanical properties of spark plasma sintered hydroxyapatites synthesized by mechanical alloying. *Ceram. Int.* **2017**, *43*, 2389–2397. [CrossRef]
17. Wang, X.; Tu, J.; Wang, C.; Zhang, X.; Chen, C.; Zhao, X. Hydrogen storage properties of nanocrystalline Mg–Ce/Ni composite. *J. Power Sources* **2006**, *159*, 163–166. [CrossRef]
18. Wang, C.; Dai, J.; Liu, W.; Zhang, L.; Wu, G. Effect of Al additions on grain refinement and mechanical properties of Mg–Sm alloys. *J. Alloys Compd.* **2015**, *620*, 172–179. [CrossRef]
19. Yang, L.; Huang, Y.; Peng, Q.; Feyerabend, F.; Kainer, K.U.; Willumeit, R.; Hort, N. Mechanical and corrosion properties of binary Mg–Dy alloys for medical applications. *Mater. Sci. Eng. B* **2011**, *176*, 1827–1834. [CrossRef]
20. Hao, H.; Ni, D.; Huang, H.; Wang, D.; Xiao, B.; Nie, Z.; Ma, Z. Effect of welding parameters on microstructure and mechanical properties of friction stir welded Al–Mg–Er alloy. *Mater. Sci. Eng. A* **2013**, *559*, 889–896. [CrossRef]
21. Lee, P.-Y.; Kao, M.C.; Lin, C.K.; Huang, J.C. Mg–Y–Cu bulk metallic glass prepared by mechanical alloying and vacuum hot-pressing. *Intermetallics* **2006**, *14*, 994–999. [CrossRef]
22. Peng, Q.; Wang, L.; Wu, Y.; Wang, L. Structure stability and strengthening mechanism of die-cast Mg–Gd–Dy based alloy. *J. Alloys Compd.* **2009**, *469*, 587–592. [CrossRef]
23. Liu, Y.; Li, K.; Luo, T.; Song, M.; Wu, H.; Xiao, J.; Tan, Y.; Cheng, M.; Chen, B.; Niu, X.; et al. Powder metallurgical low-modulus Ti–Mg alloys for biomedical applications. *Mater. Sci. Eng. C* **2015**, *56*, 241–250. [CrossRef] [PubMed]
24. Le Caër, G.; Delcroix, P.; Bégin-Colin, S.; Ziller, T. High-Energy Ball-Milling of Alloys and Compounds. *Hyperfine Interactions* **2002**, *141*, 63–72. [CrossRef]
25. Suryanarayana, C. Mechanical alloying and milling. *Prog. Mater. Sci.* **2001**, *46*, 1–184. [CrossRef]
26. Kishimura, H.; Matsumoto, H. Fabrication of Ti–Cu–Ni–Al amorphous alloys by mechanical alloying and mechanical milling. *J. Alloys Compd.* **2011**, *509*, 4386–4389. [CrossRef]
27. Qiu, W.; Pang, Y.; Xiao, Z.; Li, Z. Preparation of W-Cu alloy with high density and ultrafine grains by mechanical alloying and high pressure sintering. *Int. J. Refract. Met. Hard Mater.* **2016**, *61*, 91–97. [CrossRef]
28. Kristaly, F.; Sveda, M.; Sycheva, A.; Miko, T.; Racz, A.; Karacs, G.; Janovszky, D. Effects of milling temperature and time on phase evolution of Ti-based alloy. *J. Min. Met. Sect. B Met.* **2022**, *58*, 141–156. [CrossRef]
29. Liang, G.; Schulz, R. Synthesis of Mg–Ti alloy by mechanical alloying. *J. Mater. Sci.* **2003**, *38*, 1179–1184. [CrossRef]
30. Wilkes, D.; Goodwin, P.; Ward-Close, C.; Bagnall, K.; Steeds, J. Solid solution of Mg in Ti by mechanical alloying. *Mater. Lett.* **1996**, *27*, 47–52. [CrossRef]
31. Fecht, H.J.; Hellstern, E.; Fu, Z.; Johnson, W.L. Nanocrystalline metals prepared by high-energy ball milling. *Met. Trans. A* **1990**, *21*, 2333–2337. [CrossRef]
32. Salur, E.; Acarer, M.; Şavkliyildiz, I. Improving mechanical properties of nano-sized TiC particle reinforced AA7075 Al alloy composites produced by ball milling and hot pressing. *Mater. Today Commun.* **2021**, *27*, 102202. [CrossRef]
33. Révész, Á.; Gajdics, M. Improved H-Storage Performance of Novel Mg-Based Nanocomposites Prepared by High-Energy Ball Milling: A Review. *Energies* **2021**, *14*, 6400. [CrossRef]
34. Salleh, E.M.; Ramakrishnan, S.; Hussain, Z. Synthesis of Biodegradable Mg–Zn Alloy by Mechanical Alloying: Effect of Milling Time. *Procedia Chem.* **2016**, *19*, 525–530. [CrossRef]
35. Razzaghi, M.; Kasiri-Asgarani, M.; Bakhsheshi-Rad, H.R.; Ghayour, H. Microstructure, mechanical properties, and in-vitro biocompatibility of nano- NiTi reinforced Mg–3Zn–0.5Ag alloy: Prepared by mechanical alloying for implant applications. *Compos. Part B Eng.* **2020**, *190*, 107947. [CrossRef]
36. Salur, E.; Nazik, C.; Acarer, M.; Şavklıyıldız, I.; Akdoğan, E.K. Ultrahigh hardness in Y_2O_3 dispersed ferrous multicomponent nanocomposites. *Mater. Today Commun.* **2021**, *28*, 102637. [CrossRef]
37. Salur, E.; Aslan, A.; Kuntoğlu, M.; Acarer, M. Effect of ball milling time on the structural characteristics and mechanical properties of nano-sized Y_2O_3 particle reinforced aluminum matrix composites produced by powder metallurgy route. *Adv. Powder Technol.* **2021**, *32*, 3826–3844. [CrossRef]
38. Al, S.; Iyigor, A. Structural, electronic, elastic and thermodynamic properties of hydrogen storage magnesium-based ternary hydrides. *Chem. Phys. Lett.* **2020**, *743*, 137184. [CrossRef]
39. Wang, R.; Fang, C.; Xu, Z.; Wang, Y. Correlation of milling time with phase evolution and thermal stability of Mg-25 wt%Sn alloy. *J. Alloys Compd.* **2022**, *891*, 162014. [CrossRef]
40. Son, H.-T.; Lee, J.-B.; Jeong, H.-G.; Konno, T.J. Effects of Al and Zn additions on mechanical properties and precipitation behaviors of Mg–Sn alloy system. *Mater. Lett.* **2011**, *65*, 1966–1969. [CrossRef]
41. Poddar, P.; Sahoo, K.L.; Mukherjee, S.; Ray, A.K. Creep behaviour of Mg–8% Sn and Mg–8% Sn–3% Al–1% Si alloys. *Mater. Sci. Eng. A* **2012**, *545*, 103–110. [CrossRef]
42. Celikyürek, I.; Baksan, B.; Torun, O.; Arıcı, G.; Özcan, A. The Microstructure and Mechanical Properties of Friction Welded Cast Ni_3Al Intermetallic Alloy. *Trans. Indian Inst. Met.* **2018**, *71*, 775–779. [CrossRef]
43. Mendis, C.L.; Bettles, C.J.; Gibson, M.A.; Gorsse, S.; Hutchinson, C.R. Refinement of precipitate distributions in an age-hardenable Mg–Sn alloy through microalloying. *Philos. Mag. Lett.* **2006**, *86*, 443–456. [CrossRef]

44. Pradeep, N.; Hegde, M.R.; Rajendrachari, S.; Surendranathan, A. Investigation of microstructure and mechanical properties of microwave consolidated TiMgSr alloy prepared by high energy ball milling. *Powder Technol.* **2022**, *408*, 117715. [CrossRef]
45. Demirel, A.; Çetin, E.C.; Karakuş, A.; Ataş, M.; Yildirim, M. Microstructural Evolution and Oxidation Behavior of Fe–4Cr–6Ti Ferritic Alloy with Fe_2Ti Laves Phase Precipitates. *Arch. Met. Mater.* **2022**, *67*, 827–836. [CrossRef]
46. Yogamalar, R.; Srinivasan, R.; Vinu, A.; Ariga, K.; Bose, A.C. X-ray peak broadening analysis in ZnO nanoparticles. *Solid State Commun.* **2009**, *149*, 1919–1923. [CrossRef]
47. Miranda, M.A.R.; Sasaki, J.M.; Sombra, A.S.B.; Silva, C.C.; Remédios, C.M.R. Characterization by X ray diffraction of mechanically alloyed tripotassium sodium sulfate. *Mater. Res.* **2006**, *9*, 243–246. [CrossRef]
48. Sübütay, H.; Şavklıyıldız, I. The relationship between structural evolution and high energy ball milling duration in tin reinforced Mg alloys. *Mater. Today Commun.* **2023**, *35*, 105868. [CrossRef]
49. Shahmoradi, Y.; Souri, D.; Khorshidi, M. Glass-ceramic nanoparticles in the Ag_2O–TeO_2–V_2O_5 system: Antibacterial and bactericidal potential, their structural and extended XRD analysis by using Williamson–Smallman approach. *Ceram. Int.* **2019**, *45*, 6459–6466. [CrossRef]
50. Alshammari, Y.; Yang, F.; Bolzoni, L. Mechanical properties and microstructure of Ti–Mn alloys produced via powder metallurgy for biomedical applications. *J. Mech. Behav. Biomed. Mater.* **2019**, *91*, 391–397. [CrossRef]
51. Chaudhri, M. Subsurface strain distribution around Vickers hardness indentations in annealed polycrystalline copper. *Acta Mater.* **1998**, *46*, 3047–3056. [CrossRef]
52. Oral, I.; Kocaman, S.; Ahmetli, G. Characterization of unmodified and modified apricot kernel shell/epoxy resin biocomposites by ultrasonic wave velocities. *Polym. Bull.* **2023**, *80*, 5529–5552. [CrossRef]
53. Oral, I.; Ekrem, M. Measurement of the elastic properties of epoxy resin/polyvinyl alcohol nanocomposites by ultrasonic wave velocities. *Express Polym. Lett.* **2022**, *16*, 591–606. [CrossRef]
54. Altintas Yildirim, O.; Atas, M.S. Synthesis and characterization of spherical $FeNi_3$ metallic nanoparticles based on sodium dodecyl sulfate. *J. Mater. Manuf.* **2022**, *1*, 33–40.
55. Frost, M.; McBride, E.E.; Schörner, M.; Redmer, R.; Glenzer, S.H. Sodium-potassium system at high pressure. *Phys. Rev. B* **2020**, *101*, 224108. [CrossRef]
56. Şavklıyıldız, İ.; Akdoğan, E.K.; Zhong, Z.; Wang, L.; Weidner, D.; Vaughan, M.; Croft, M.C.; Tsakalakos, T. Phase transformations in hypereutectic MgO–Y_2O_3 nanocomposites at 5.5 GPa. *J. Appl. Phys.* **2013**, *113*, 203520. [CrossRef]
57. Şavkliyildiz, İ. In-Situ Strain Measurement on Al7075 Plate by Using High Energy Synchrotron Light Source. *Avrupa Bilim Ve Teknol. Derg.* **2021**, *23*, 435–439.
58. Akdoğan, E.K.; Şavkliyildiz, İ.; Berke, B.; Zhong, Z.; Wang, L.; Vaughan, M.; Tsakalakos, T. High-pressure phase transformations in MgO–Y_2O_3 nanocomposites. *Appl. Phys. Lett.* **2011**, *99*, 141915. [CrossRef]
59. Akdoğan, E.; Şavkliyildiz, İ.; Berke, B.; Zhong, Z.; Weidner, D.; Croft, M.C.; Tsakalakos, T. Pressure effects on phase equilibria and solid solubility in MgO–Y_2O_3 nanocomposites. *J. Appl. Phys.* **2012**, *111*, 053506. [CrossRef]
60. Gehrmann, R.; Frommert, M.M.; Gottstein, G. Texture effects on plastic deformation of magnesium. *Mater. Sci. Eng. A* **2005**, *395*, 338–349. [CrossRef]
61. Nayyeri, M.J.; Ganjkhanlou, Y.; Kolahi, A.; Jamili, A.M. Effect of Ca and Rare Earth Additions on the Texture, Microhardness, Microstructure and Structural Properties of As-Cast Mg–$_4$Al–$_2$Sn Alloys. *Trans. Indian Inst. Met.* **2014**, *67*, 469–475. [CrossRef]
62. Huot, J.; Skryabina, N.Y.; Fruchart, D. Application of Severe Plastic Deformation Techniques to Magnesium for Enhanced Hydrogen Sorption Properties. *Metals* **2012**, *2*, 329–343. [CrossRef]
63. Atas, M.S.; Yildirim, M. Morphological development, coarsening, and oxidation behavior of Ni–Al–Nb superalloys. *J. Mater. Eng. Perform.* **2020**, *29*, 4421–4434. [CrossRef]
64. Ye, H.Z.; Liu, X.Y. Review of recent studies in magnesium matrix composites. *J. Mater. Sci.* **2004**, *39*, 6153–6171. [CrossRef]
65. Chen, J.; Wei, J.; Yan, H.; Su, B.; Pan, X. Effects of cooling rate and pressure on microstructure and mechanical properties of sub-rapidly solidified Mg–Zn–Sn–Al–Ca alloy. *Mater. Des.* **2013**, *45*, 300–307. [CrossRef]
66. Huang, K.; Marthinsen, K.; Zhao, Q.; Logé, R.E. The double-edge effect of second-phase particles on the recrystallization behaviour and associated mechanical properties of metallic materials. *Prog. Mater. Sci.* **2018**, *92*, 284–359. [CrossRef]
67. Sun, S.; Deng, N.; Zhang, H.; He, L.; Zhou, H.; Han, B.; Gao, K.; Wang, X. Microstructure and mechanical properties of AZ31 magnesium alloy reinforced with novel sub-micron vanadium particles by powder metallurgy. *J. Mater. Res. Technol.* **2021**, *15*, 1789–1800. [CrossRef]
68. Li, Y.; Chen, C.; Deng, R.; Feng, X.; Shen, Y. Microstructure evolution of Cr coatings on Cu substrates prepared by mechanical alloying method. *Powder Technol.* **2014**, *268*, 165–172. [CrossRef]
69. Bamberger, M.; Dehm, G. Trends in the Development of New Mg Alloys. *Annu. Rev. Mater. Res.* **2008**, *38*, 505–533. [CrossRef]
70. Arici, G.; Acarer, M.; Uyaner, M. Effect of Co addition on microstructure and mechanical properties of new generation 3Cr-3W and 5Cr-3W steels. *Eng. Sci. Technol. Int. J.* **2021**, *24*, 974–989. [CrossRef]